Data Mine

Active and Passive Seismic Surveys over the Grounding Zone of Eastwind Glacier, Antarctica

Ronan S. Agnew*†[1,2], Emma Pearce†[2,3], Marianne Karplus[4], Meghana Ranganathan[5], Andrew O. Hoffman[6], Madeline Hunt[7,8], Andrew Pretorius[1], Sooraj E. Shanly[1,9], Mitchel Beres[10], Kaushik K. Pradhan[4], Yeshey Seldon[4,11], Adam D. Booth[1], Roger A. Clark[1], and Tun Jan Young[12]

Abstract

The grounding zone of a marine-terminating glacier, where ice begins to float, is a key control on glacier stability and ice discharge. Seismic deployments are a powerful means of studying both the geometry and processes of grounding zones; however, these regions are frequently inaccessible and dangerous for field work, and as a result are underrepresented in field studies. We report new data sets acquired at Eastwind Glacier, Antarctica, a relatively accessible grounding zone near McMurdo Station and Scott Base, as part of the Eastwind Glacier Geophysical Surveys on Top of an Antarctic Ice Shelf Transition, EGGS on TOAST, project. These data sets comprise a deployment of three-component seismic nodes and distributed acoustic sensing. The nodal deployment consisted of 330 nodes crossing the grounding zone, with all 330 nodes continuously recording for at least nine days, and 150 nodes recording for 19 days, in the austral summer of 2022/2023. Hammer-and-plate sources were recorded, with densely spaced shots along flow through the center of the array and shots located at every node. In 2023/2024, a 2.2 km fiber-optic cable was deployed for active source imaging by distributed acoustic sensing along and across flow, immediately downstream of the grounding line, for a period of 2 hr. Analysis of active source data recorded by the nodal array locates the point of flotation within the grounding zone and provides ice thickness estimates. We present initial analyses of passive source data, including icequake detection and location, and ambient noise analysis. We expect this data set to be of significant value to provide insight into fundamental grounding zone processes and as an event-rich cryoseismological data set on which to test novel methods of seismic analysis.

Cite this article as Agnew, R. S., E. Pearce, M. Karplus, M. Ranganathan, A. O. Hoffman, M. Hunt, A. Pretorius, S. E. Shanly, M. Beres, K. K. Pradhan, *et al.* (2025). Active and Passive Seismic Surveys over the Grounding Zone of Eastwind Glacier, Antarctica, *Seismol. Res. Lett.* **97**, 591–605, doi: 10.1785/0220250024.

Supplemental Material

Introduction

Dynamics of marine-terminating glaciers and ice sheets are influenced by both their geometry and physical processes at grounding zones, where the ice transitions from grounded on land to floating on water (Weertman, 1974; Hughes, 1975; Conway *et al.*, 1999; Schoof, 2007). The locations of grounding zones define the point at which ice no longer responds to friction associated with basal sliding, and are also a measure of glacier extent, bounding the interior grounded region of an ice sheet that can contribute to sea level. Glacier grounding zones are dynamic environments in which the flotation point advances and retreats in response to both short-term tidal variation (e.g., Freer *et al.*, 2023) and to longer-term glaciological and oceanographic forcings (e.g., Gudmundsson *et al.*, 2012; Robel *et al.*, 2014; Neuhaus *et al.*, 2021; Haseloff and Sergienko, 2022). Primary controls on a

1. University of Leeds, Leeds, United Kingdom, https://orcid.org/0009-0000-3609-6815 (RSA); https://orcid.org/0000-0002-8166-9608 (ADB); https://orcid.org/0000-0002-3508-8183 (RAC); 2. British Antarctic Survey, Cambridge, United Kingdom, https://orcid.org/0000-0001-5696-8465 (EP); 3. University of Strasbourg/CNRS Institut Terre and Environment of Strasbourg (ITES), Strasbourg, France; 4. University of Texas at El Paso, El Paso, Texas, U.S.A., https://orcid.org/0000-0001-6007-5790 (MK); https://orcid.org/0000-0001-7722-0106 (KKP); https://orcid.org/0009-0007-1389-2924 (YS); 5. University of Chicago, Chicago, Illinois, U.S.A., https://orcid.org/0000-0002-8099-4775 (MR); 6. Lamont-Doherty Earth Observatory, Palisades, New York, U.S.A., https://orcid.org/0000-0003-1236-5704 (AOH); 7. Earthscope Consortium, Socorro, New Mexico, U.S.A., https://orcid.org/0009-0005-6364-318X (MH); 8. Boise State University, Boise, Idaho, U.S.A.; 9. Peak Processing, Wroxham, United Kingdom; 10. Montana State University, Bozeman, Montana, U.S.A.; 11. Southern Methodist University, Dallas, Texas, U.S.A.; 12. University of St Andrews, St Andrews, Scotland, https://orcid.org/0000-0001-5865-3459 (TJY)

*Corresponding author: rognew91@bas.ac.uk

†These authors contributed equally to the work.

glacier grounding zone include the glacier geometry and ice volume, bed characteristics beneath the glacier, sea level and ocean tidal effects, and sea floor topography and materials (Fricker *et al.*, 2009; Brunt *et al.*, 2010).

Numerous observational studies have suggested that present-day grounding zones across the Antarctic ice sheet are in long-term retreat, increasing their contribution to sea-level rise and potentially influencing instabilities that could affect large portions of the ice sheet (Joughin *et al.*, 2014; Rignot *et al.*, 2014; Jenkins *et al.*, 2018; Graham *et al.*, 2022; Reese *et al.*, 2023). These observations make mapping and understanding grounding zone processes of great importance to understand the present and future behavior of the Antarctic ice sheet. Geophysical techniques are valuable tools with which to observe these processes.

In recent years, dense seismic monitoring of glaciers has become increasingly commonplace because technological advances now make it possible to deploy large numbers (100 s–1000 s) of three-component, lightweight seismic nodes on glaciers; these include geophones and digitizers with built-in batteries lasting up to 35 days (e.g., Karplus and Schmandt, 2018; Gimbert *et al.*, 2021; Veitch *et al.*, 2021; Nanni *et al.*, 2022; Karplus *et al.*, 2024). Using data from these networks, a suite of seismic imaging methods can be used to improve our understanding of glacier structure and processes. This includes analysis of impulsive sources such as icequakes and of ambient noise. Icequakes are microseismic events associated with basal stick-slip or englacial fracturing and are a widespread phenomenon; basal seismicity beneath marine-terminating glaciers and ice streams has been linked to tidal cycles (e.g., Anandakrishnan and Alley, 1997; Zoet *et al.*, 2012; Podolskiy *et al.*, 2016; Minowa *et al.*, 2019; Lucas *et al.*, 2023). Studying icequakes using dense seismic networks has provided insight into glacier basal stick-slip mechanics (Gimbert *et al.*, 2021), crevasse location (Nanni *et al.*, 2022), and ice deformation at a grounding zone related to tidal cycles (Le Bris *et al.*, 2024). Ambient noise sources have been used to study subglacial hydrology (van Ginkel *et al.*, 2025), as well as the structure and anisotropy of firn and ice (Chaput *et al.*, 2023; Pearce *et al.*, 2024). Using ambient noise techniques with a dense seismic array, Nanni *et al.* (2021) demonstrated the potential of dense seismic monitoring to study the subglacial environment, mapping a subglacial hydrological system in great detail. A dense array spanning a glacier grounding zone therefore has the potential to provide insight into the complex processes occurring in and beneath the ice in this dynamic environment and to investigate structural features of the ice column.

Distributed acoustic sensing (DAS) is a complementary method to traditional seismic deployments. Fiber-optic cables can be deployed on the surface or in pre-existing boreholes, offering an efficient means to investigate glacial structures at extremely high resolution. In Greenland and Antarctica, fiber-optic methods have been used to record anthropogenic noise (Fichtner, Hofstede, Kennett, *et al.*, 2023), and for active-source surveying (Booth *et al.*, 2020; Brisbourne *et al.*, 2021; Fichtner, Hofstede, Gebraad, *et al.*, 2023) to constrain internal ice structure and basal properties. Other workers have used naturally occurring seismicity to monitor englacial deformation (Fichtner *et al.*, 2025) and basal processes (Hudson *et al.*, 2021), demonstrating the versatility of DAS as a glacier geophysical tool (see Brisbourne *et al.*, 2024, for an overview of recent advances in glaciological DAS studies).

Although field geophysical campaigns on Antarctic ice streams have advanced our understanding of grounding zones (Anandakrishnan *et al.*, 2003; Christianson *et al.*, 2013; Hulbe *et al.*, 2016; Horgan *et al.*, 2021; Davis *et al.*, 2023), many questions remain about ice–ocean interactions, ice mechanics, and sediment deposition in these environments (Begeman *et al.*, 2020; Drews *et al.*, 2021; Davis *et al.*, 2023). In this article, we describe data collected as part of the Eastwind Glacier Geophysical Surveys oN Top of an Antarctic Ice Shelf Transition, EGGS on TOAST, project. The project aims to investigate the geometry and processes of the grounding zone of Eastwind Glacier using active- and passive-source seismic and DAS data collected over two field seasons during the 2022–2023 and 2023–2024 austral summers. Ice-penetrating radar and geodetic data were also collected during the same season and are reported elsewhere (Hoffman *et al.*, 2025). We selected this suite of techniques to illuminate all parts of the grounding zone, including the snow, firn, ice, bed, ocean, and seafloor, in detail and in three dimensions. Although there is a long history of seismic recording on and near Ross Island (Stern *et al.*, 1991; Rowe *et al.*, 2000), this is the first seismic deployment on Eastwind Glacier (EG) and the first seismic survey crossing the grounding zone of a Ross Island glacier. We believe this deployment is the most extensive nodal array to date at a glacier grounding zone.

Study Area

EG is an ~30 km^2 glacier that drains the south slope of Mount Terror on Ross Island flowing with a maximum velocity of ~300 m yr^{-1} (Fig. 1). It flows southwest from Mount Terror before merging with Terror Glacier along its western edge and flowing into Fog Bay, a small bay in Windless Bight, feeding the McMurdo Ice Shelf. Ross Island is located near the southern end of the Terror rift within the West Antarctic rift system (Behrendt, 1999). The island formed with the emplacement of basaltic shield volcanoes Mount Bird (1765 m) and Mount Terror (3230 m) between 4.6 and 3.8 Ma and 1.7 and 1.3 Ma, respectively, and has continued to evolve over the past 1 Ma with the formation of the ~3795 m high composite edifice of Mount Erebus during its current eruptive phase. The persistent convecting lava lake near the summit of Erebus is connected to a magma-filled conduit system with surface vents and fumaroles, which contributes to various eruptive seismic signals, including very long-period signals (Aster *et al.*, 2003; Dibble *et al.*, 2008).

Figure 1 shows the study area in the wider context of Ross Island and the Antarctic continent. The grounding zone of EG

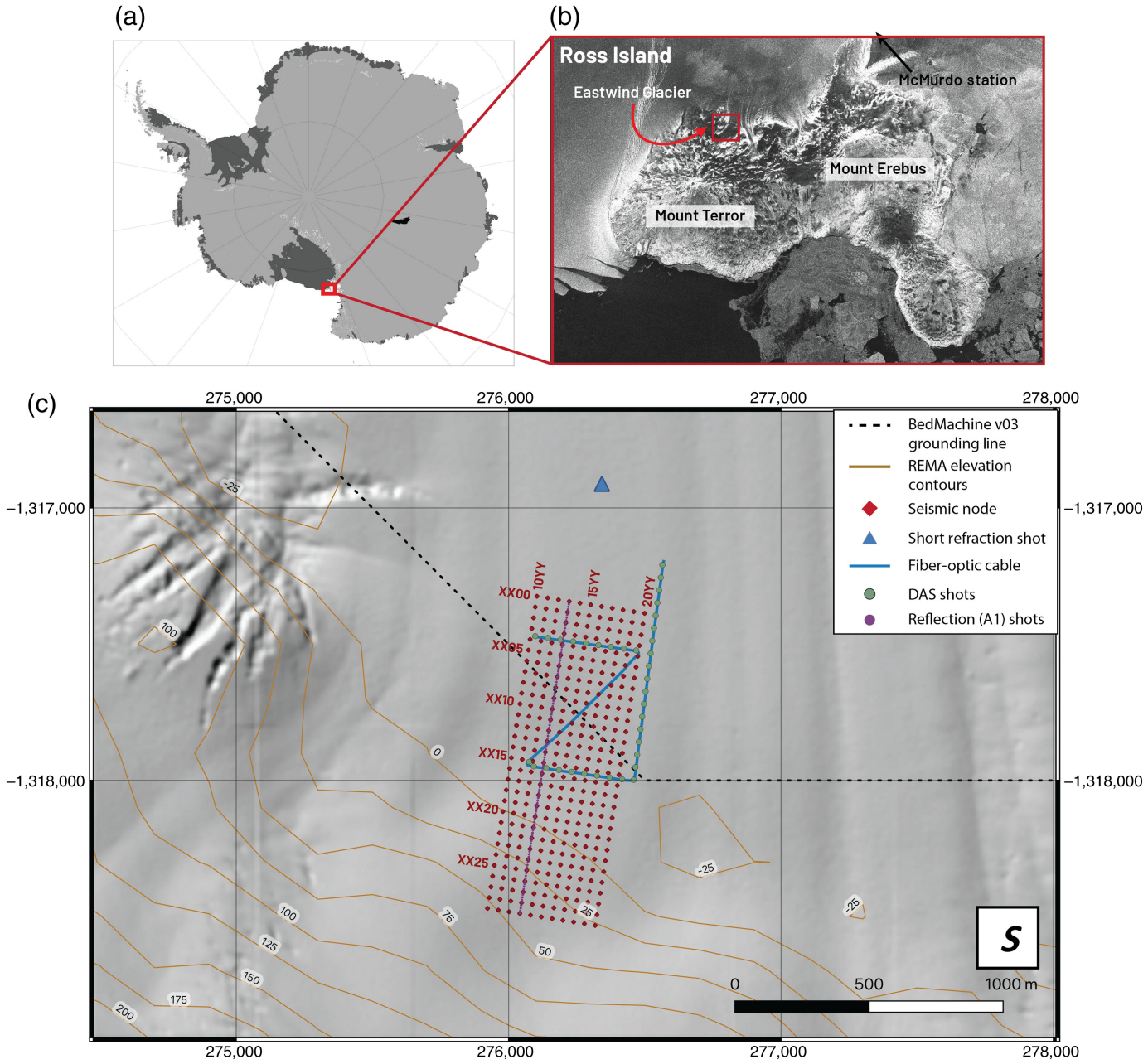

Figure 1. (a) Map of Antarctica from Morlighem *et al.* (2020), with grounded ice in light gray, floating ice in dark gray, and Ross Island denoted by a red box. (b) Map of Ross Island, with Eastwind Glacier denoted by a red box. Imagery is from Sentinel 1A data, converted to reflection backscatter using the SNAP toolbox. (c) Topographic map of the study area, with ice flow from bottom to top. The dotted arrow points in the direction of flow. Locations of seismic nodes are shown by red diamonds, and seismic reflection shot points (acquisition A1) are shown by purple dots. Also shown are the distributed acoustic sensing (DAS) cable (blue line) and associated shots (green dots) and shot location for short refraction survey (blue triangle). Surface elevation contours are from the reference elevation model for Antarctica (REMA; Howat *et al.*, 2019). The grounding line shown is from BedMachine v03 (Morlighem *et al.*, 2020; Morlighem *et al.*, 2022). Note this grounding line is downstream of the topographic minimum and expected grounding line from surface topography. The color version of this figure is available only in the electronic edition.

is ~5 km north from "Cozy Camp" (77.693° S 168.087° E), ~50 km from Scott Base and McMurdo stations, and it is easily accessible by snowmobile and PistenBully. The main trunk of the glacier is ~1.5 km wide, and its shear margins contain active crevassing and icefall features. Despite this, there is a limited surface crevassing on the main trunk of the glacier and nearby shelf, so the area is therefore relatively safe for in situ geophysical surveying compared with other grounding zones, which frequently exhibit more deformation and surface crevassing. This study area was chosen due to its relative

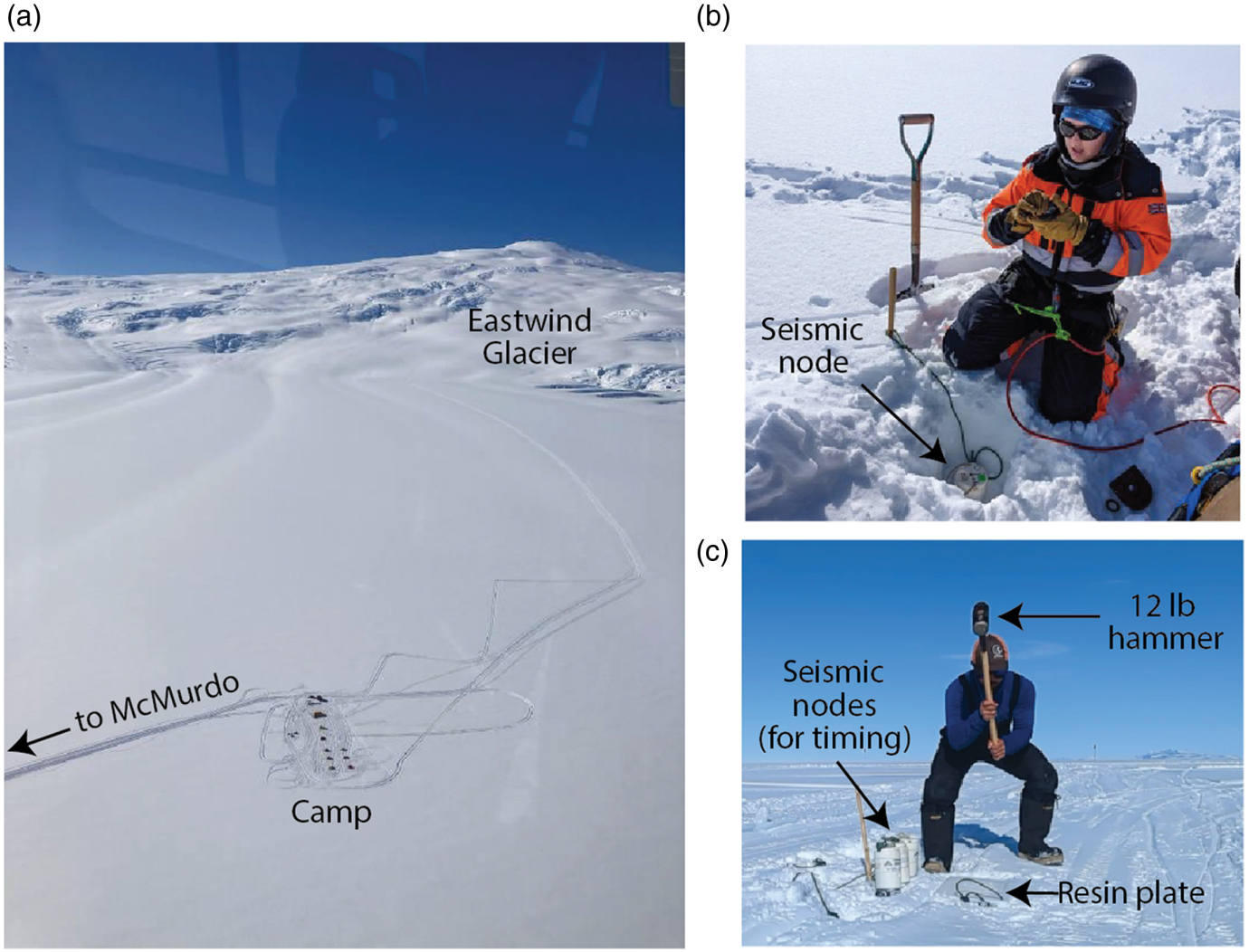

Figure 2. (a) Aerial photo of Cozy Camp, with vehicle track leading to Eastwind Glacier and the nodal array (Photograph credit: Jenny Cunningham). (b) Field deployment of a three-component seismic node at ~25 cm depth. (c) Hammer strikes on resin plate to create seismic source, with timing nodes nearby. The color version of this figure is available only in the electronic edition.

accessibility, safety, scale, and the ability to observe a complete grounding zone with relative logistical simplicity.

Data Acquisition and Availability

Nodal array

During the first field season (2022–2023), we deployed a nodal array across the grounding zone of EG, as defined loosely from surface topography and supported by ice-penetrating radar data acquired in late 2022 (Hoffman *et al.*, 2025). An expected grounding line position was identified upstream of a minimum in surface elevation, which occurs where ungrounded ice forms a depression immediately downstream of the flotation point before adjusting to isostatic equilibrium. It was therefore expected that the array would span both grounded ice and ice shelf.

A total of 330 Magseis Fairfield Z-Land Generation 25 Hz three-component nodes were deployed in an array between 11 and 13 January 2023 (Fig. 2). The nodes were deployed in eleven lines aligned along the flow of the glacier, with the naming convention of XXYY, in which XX represents the across flow line number. YY represents the position along flow in that line, sequenced opposite to the flow direction (i.e., station XX00 is positioned farthest downstream in line XX). Each line was composed of 30 nodes. Nodes were spaced 40 m apart in both the along- and across-flow directions to allow sufficient spatial coverage both along and across flow, while also allowing the recovery of wavelengths down to 80 m; this is sufficient for the recording and use of ambient noise data to image the shallow subsurface. The array spanned a 400 m by 1160 m grid covering the approximate location of the grounding zone, with the true north end of the grid upstream on the grounded ice and the south end of the grid downstream on the ice shelf. All nodes recorded at a sampling rate of 1 kHz and a preamp gain of 12 dB. Nodes were oriented to true north using a magnetic declination of 138° E and buried at an average depth of 25 cm

TABLE 1
Timeline of Activities Conducted at the Field Site in January/February 2023

Date (mm/dd)	Activity
01/11–01/13	Installed seismic nodes
01/14–01/16	Refraction survey (Hoffman *et al.*, 2025)
01/16	Snowmobile grooming of survey region
01/17	2D active source survey (acquisition A1)
01/18–01/21	3D active source survey (acquisition A2)
01/22	Decommissioned 180 seismic nodes
01/23	Camp pullout
01/24–01/31	Seismic nodes recording for "quiet period"
02/01–02/02	Uplift of remaining seismic nodes

from the snow surface to the top of the node. Bamboo poles were installed roughly 0.5 m west of each node to mitigate wind noise, and a 1.5 m length of string was tied between the bamboo and the node to aid in rapid node recovery (Fig. 2b). All stations were located using a real-time kinematic (RTK) Global Navigation Satellite Systems receiver (Stonex S900) prior to node deployment, with relative positions to a base station located at station 1414 determined to within a few centimeters. A timeline of activity around the deployment is shown in Table 1.

One hundred eighty nodes (along-flow lines 13, 14, 15, 17, and 18; stations 13YY, 14YY, 15YY, 17YY, 18YY, and 19YY) were retrieved on 22 January 2023, after 9–11 days of recording. The remaining 150 nodes (lines 10YY, 11YY, 12YY, 16YY, and 20YY) were retrieved on 1–2 February 2023, after 19–22 days of recording. Nodes retrieved on 22 January were chosen to maximize variation of distances between remaining stations. Data were offloaded in Fairfield continuous (fcnt) format and then converted to PH5 format using Earthscope PH5 tools. All PH5 data are archived at the Earthscope Data Management Center with the network code XS (Young *et al.*, 2023).

Active source experiments

The January–February 2023 nodal array was designed to facilitate joint passive and active acquisitions. Sources were generated by a 12 lb sledgehammer striking a 30 × 30 × 2 cm resin plate placed at the snow surface (Fig. 2c). At least five good-quality hammer strikes (good coupling with the plate and no double bounce of the hammer) were conducted at each source location. A node was deployed (station number 1334) at each source location and carried between source locations to record shot times at zero offset. Source times were recorded to the nearest second, so the exact time must be estimated from the timer node record in further analysis. Hammer strikes were at least 10 s apart to ensure the individual shots could be identified in the seismic record without interference from adjacent shots in the sequence.

Data from two groups of seismic sources, which we refer to as A1 and A2, were recorded at the node grid: (A1) a 2D reflection profile and (A2) a 3D acquisition. The 2D reflection profile (A1) was acquired along line 13 of the node grid on 17 January 2023 and consisted of a total of one hundred seventeen sources, spaced at 10 m intervals between stations 1300 and 1329. The sources for acquisition A2 were located at every station in the node grid along lines 10 to 20 (330 source locations in total). These data were collected from 18–21 January 2023. In addition to this, short refraction surveys, recorded with conventional geophones on a Geometrics Geode system, were conducted on 14–16 January 2023 and are reported by Hoffman *et al.* (2025).

DAS

During the second field season (2023–2024), we acquired DAS seismic data along a fiber-optic cable, immediately downstream of the grounding line. We deployed ∼2.2 km of Linden SPE-7196 single-mode fiber-optic cable using a fiber-optic cable-laying sled towed behind a snowmobile. The sled included a spool holding the fiber-optic cable and a metal keel with a hollow metal tube to simultaneously dig a trench 30 cm deep and unspool the cable into the trench as the sled was towed. The fiber-optic cable was deployed in a layout that provides seismic recording parallel to the long and short axes of the 2022–2023 nodal grid (Fig. 1). The first section of cable extended in a northerly direction from the interrogator, parallel to the long axis of the grid, then turned east to cross its short axis. The cable then tracked diagonally southwest across the grid, with a final span again traversing east across the short axis of the grid close to its southern extent. The total length of fiber-optic cable is 3.4 km. This comprises, in order, (1) a 1 km launch lead (included to ensure faithful recording of amplitudes along the whole cable length), (2) the main 2.2 km of fiber under test, and (3) 200 m of redundant fiber remaining spooled on a cable drum. Channels 1–625 therefore compose launch lead and channels 2076–2200 compose redundant cable. The cable was buried on 5 February 2024 and left for two days to sinter in to improve coupling to the soft snow.

On 7 February 2024, we recorded continuous data with a Febus Optics A1-R interrogator over a 2 hr period. The system was powered by a 2 kHz portable generator with an uninterruptable power supply, which set a limit on continuous recording time due to the necessity of refueling. The interrogator and PC monitor were kept in a tent to keep snow out and keep the system warm. Because the cable was trenched at a consistent depth in the snow to isolate it from wind noise, we expect coupling and noise to be consistent along the cable, and reflective of the coupling achieved by the nodes buried at approximately the same depth. Generator noise was mitigated by placing the

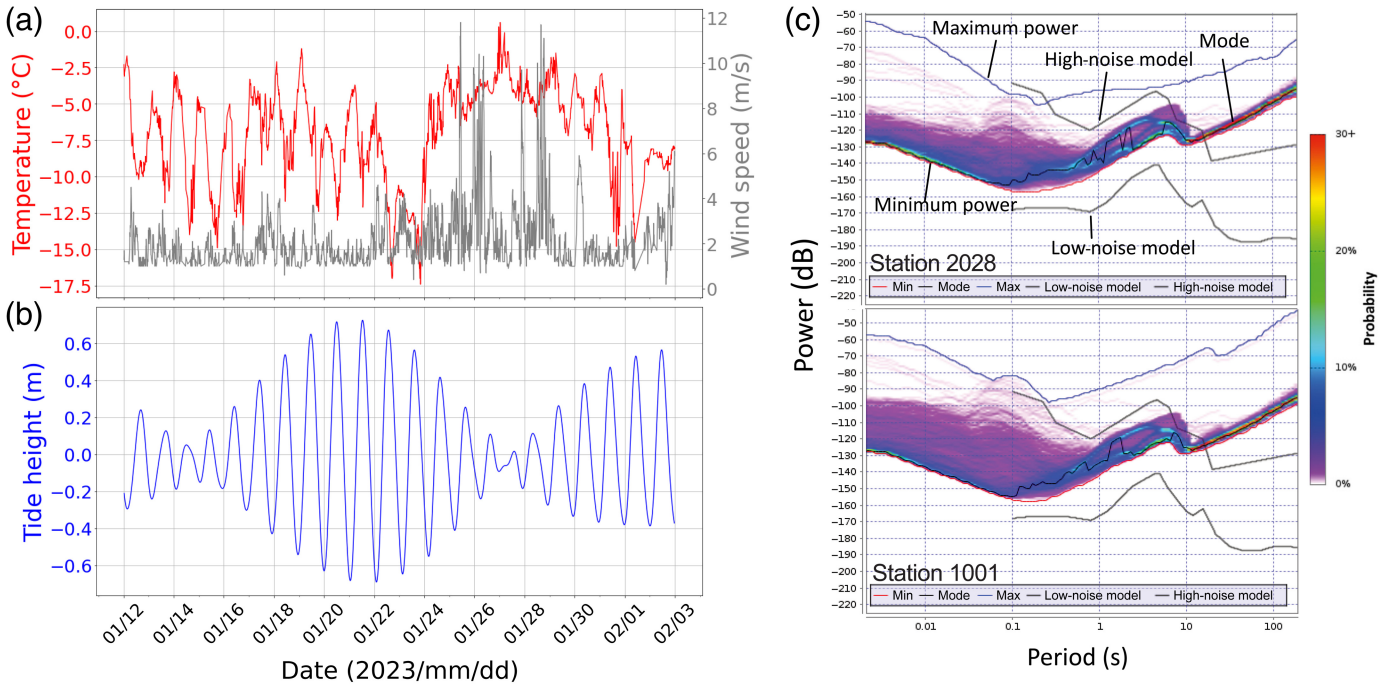

Figure 3. (a) Wind speed and temperature for the 2023 period of node deployment, from the Windless Bight Automatic Weather Station. (b) Tidal data for the period of node deployment, from the CATS2008 tidal model (Padman *et al.*, 2002). (c) Noise probability density functions (PDFs) derived from power spectral density (PSD) for vertical components across all stations, from the Incorporated Research Institutions for Seismology (IRIS) Modular Utility for STAtistical kNowledge Gathering (Casey *et al.*, 2018). The color scale represents the probability density of a specific power level at a certain frequency. The red line represents the minimum power at each period, the blue line represents the maximum power, and the black line represents mode. The brown lines represent a low- and high-noise model for the entire array (Peterson, 1993). The color version of this figure is available only in the electronic edition.

generator on foam pads and situating it roughly 15 m from the end of the fiber. The measurement of strain rate was calculated in a 10 m gauge length. The output data set has a 1 ms sampling interval and a 1.6 m trace interval.

Hammer strikes were recorded at thirty-six locations along the length of the fiber-optic cable, with a distance of 47 m between the shot locations, and no shots recorded along the diagonal section of the cable (Fig. 1). Shot points were surveyed by RTK Global Positioning System (GPS). Up to seven repeat shots were taken at each location to facilitate stacking and increase signal-to-noise ratio (SNR). Shot times are estimated directly from the DAS data, which has GPS timing, by observing the earliest arrival of seismic energy at the appropriate position along the cable. DAS data are available at the United Kingdom Natural Environment Research Council Polar Data Centre.

Environment

As context for further analyses of the nodal data acquired in January–February 2023, we show data from the Windless Bight Automatic Weather Station (Lazzara *et al.*, 2012), along with tidal data obtained from the CATS2008 high-resolution regional inverse model of the entire circum-Antarctic ocean (Padman *et al.*, 2002). The deployment covered most of the period of a spring-neap tidal cycle and hence could record signals due to tidal mixing or grounding line migration associated with the change in tide height (e.g., Minowa *et al.*, 2019; Nanni *et al.*, 2022).

Figure 3a,b shows a summary of wind speed, temperature, and tide height for the period of deployment. Temperatures ranged from −17.4°C to +0.6°C, averaging −7°C ± 3°C. Wind speeds ranged from 0.2 to 11.8 m s^{-1}, with maximum speeds recorded between 25 and 29 January. The average wind speed for the period of node deployment was 2.4 m s^{-1}. During node retrieval, we noted that more than 30 cm of snow had accumulated on top of the nodes between 23 January and 1 February 2023. Nodes were deployed for the majority of a monthly tidal cycle, with a maximum tidal amplitude of 1.4 m.

Figure 3c shows aggregated noise probability density functions (PDFs) for representative "quiet" (station 2028) and "noisy" (station 1001) stations for the period of deployment. The PDF is derived from power spectral density estimates (McNamara and Buland, 2004) for the nodes using the method of Casey *et al.* (2018). Lines representing models of typical global background seismic noise are plotted alongside the PDF and are marked as "high noise model" and "low noise model" (Peterson, 1993). The maximum and minimum power as a function of period are shown as the blue and red lines, respectively. The primary microseism peak, likely produced by the direct interaction of ocean waves with the coastline, is probably obscured by the self-noise of the nodes. The

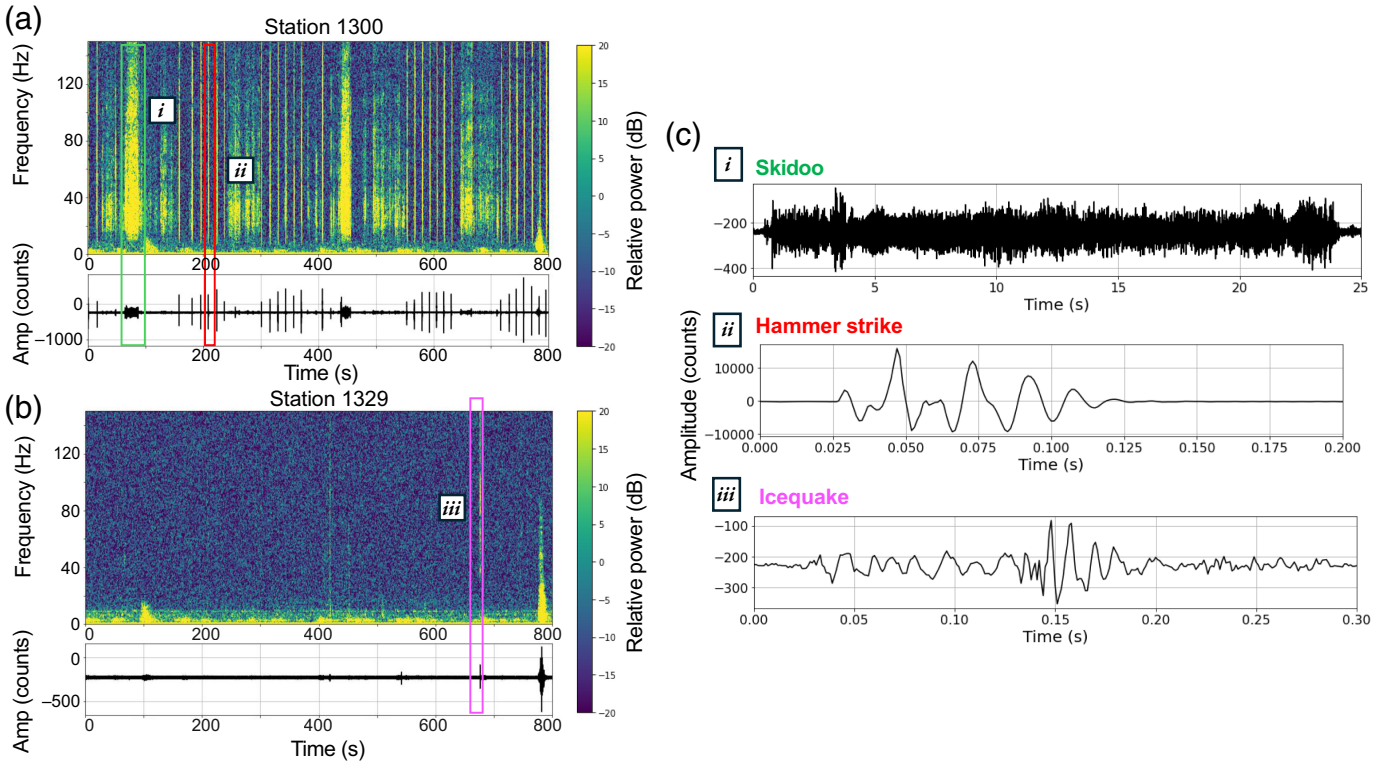

Figure 4. Example signals recorded by the deployed array on 17 January 2023. (i) Skidoo noise, (ii) Hammer strike from active source surveying, and (iii) icequake. (a,b) Spectrograms and vertical-component traces for stations 1300 (downstream) and 1329 (upstream) for the exact same time period. Plots on the right side (c) show a zoom of the event signals (vertical component). Skidoo and hammer strike traces are shown from station 1300. Icequake signal is shown from station 1329. The color version of this figure is available only in the electronic edition.

secondary microseism (half the period of the primary) results from the interaction of direct and reflected ocean waves (Longuet-Higgins, 1950) and can be seen at a period of ~5–10 s. The PDF from these data generally falls between the low- and high-noise models (Peterson, 1993) for the expected frequencies for the nodes, indicating generally expected background noise levels for the sensors.

Data Snapshots

Example events

A wide variety of seismic signals were recorded by the nodal array; examples are shown in Figure 4. Figure 4a,b shows spectrograms for an 800 s period on 17 January 2023, for stations 1300 and 1329, which are at opposite ends of the array (downstream/upstream, respectively). The signals shown for this time period include both active (i, ii) and passive source (iii, iv) signals. Event (i) consists of skidoo noise, and (ii) shows a hammer-and-plate source. We interpret signal (iii) as an icequake, recorded only at the upstream station (over grounded ice).

Seismic reflection (hammer-and-plate node data)

Shot times were precisely found by picking shots from the timer node record. Shot gathers were then extracted from the PH5 volume and stacked to improve the SNR. Data were then processed as common receiver gathers because of the unconventional shooting geometry combining sparse receiver coverage with dense source spacing. Preprocessing followed a workflow that involved static corrections to correct for surface topography, spiking deconvolution (minimum phase, operator length 20 ms), and frequency–wavenumber (*f-k*) filtering to remove interference from groundroll. The *f-k* filter was chosen to remove phases with apparent velocities less than 3.5 km s^{-1}, and 200 Hz noise with zero apparent velocity prominent on near-offset channels. An Ormsby band-pass filter (frequencies 25–50–250–300 Hz) was then applied. The dominant frequency of the reflected wavelet is 84 Hz, with a normal-incidence Fresnel radius at the ice base of ~74 m. Figure 5 shows two preprocessed common receiver gathers from the acquisition (unprocessed receiver gathers can be found in the supplemental material, available to this article). Figure 5a shows a receiver gather from station 1300, at the far downstream end of the array, assumed to be on the shelf. Inset is an example wavelet of a diving wave first arrival to highlight the polarity convention. The ice-base reflection (two-way travel time ≃0.15 s) at this point is a reversed polarity wavelet (label 1), indicating a downward change in acoustic impedance consistent with an ice–water interface. This is followed at 0.31 s by the ice–base multiple (label 2), and at 0.34 s by the normal-polarity seabed reflection (label 3). At the shelf end of the line, there is an interference between the seabed primary reflection

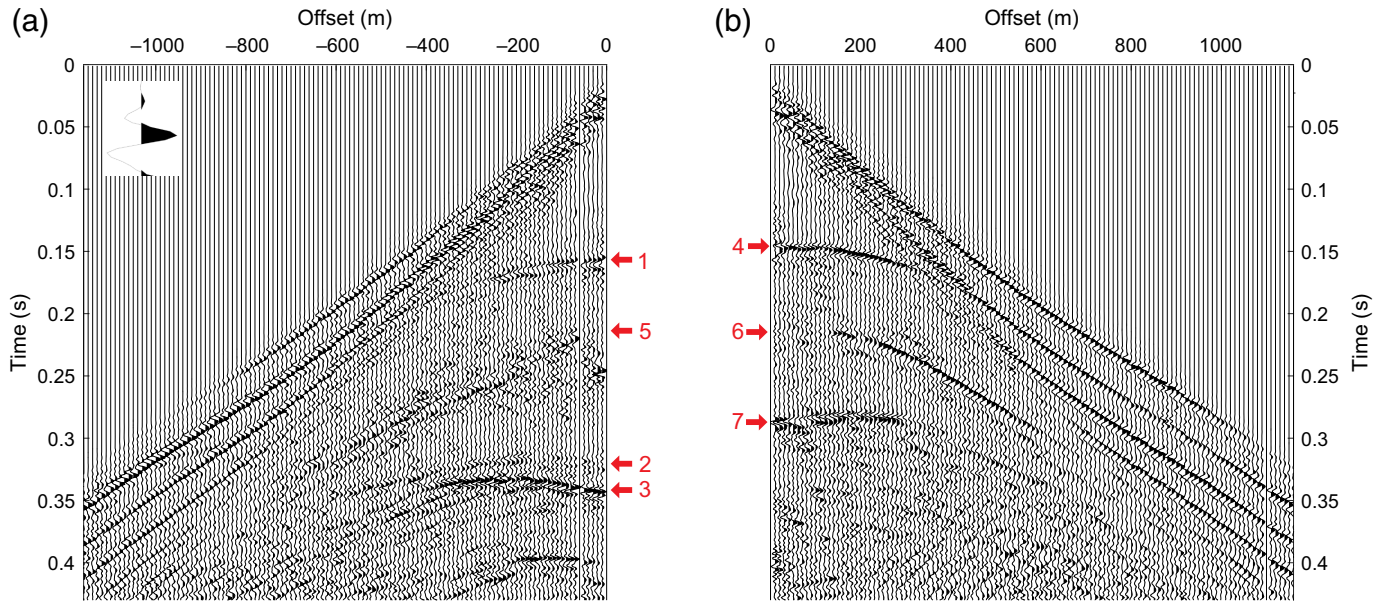

Figure 5. Common receiver gathers from (a) station 1300, at the far downstream end of the array, and (b) station 1329, at the far upstream end. Main reflected phases visible are labeled as (1) ice–water interface (reverse polarity), (2) ice–water multiple, (3) seabed reflection, (4) ice–bed interface (normal polarity), (5), (6) converted wave, and (7) ice–bed multiple. Data shown are preprocessed receiver gathers shown with an automatic gain control (window length 100 ms) for display only. Inset in (a) shows a diving wavelet to highlight the polarity convention. The color version of this figure is available only in the electronic edition.

and the ice–water first multiple. Figure 5b shows a common-receiver gather from station 1329, at the far upstream end of the line. The ice–base reflection here is of normal polarity, which is consistent with an ice–bedrock/stiff sediment interface (label 4). There is an arrival (two-way travel time ~0.2 s; label 5) with significant energy between the ice–base primary and its multiple (label 6), which may be a *P-to-S* converted wave detected on the vertical component due to the basal and surface topography.

DAS

Hammer strikes were recorded by the DAS interrogator (Fig. 6). The strain-rate response to the shot was observed in the fiber-optic cable roughly 200 m either side of the shot points. Hammer strikes are impulsive signals with frequency content from ~50 to 300 Hz. Figure 6a,b shows example windows of multichannel DAS data, along with an example of a single trace (channel 719, 9.5 m source–receiver offset), both raw and with a band-pass filter applied (Fig. 6c). Figure 6d shows a spectrogram of a recorded trace.

First Results

Reflection imaging

Preprocessed data were corrected for normal moveout and stacked. Figure 7a shows the surface topography obtained from RTK GPS surveys and Figure 7b an unmigrated time section obtained from the hammer-and-plate source node data. Ice flow is from right to left. Labeled on the section are the clearly visible ice–water and ice–bedrock interfaces (1 and 2, respectively), the seabed (3 and 4), and the ice-bottom multiple (5). Apparent features in the ice column arriving before the ice–base reflection consist of residual groundroll and *f-k* artefacts.

The grounding zone location is identifiable as the point in the profile where the ice–base reflection changes polarity from reversed to normal. We do not analyze absolute reflectivity; however, we note that the positive polarity reflection from the ice–bed interface must come from a positive impedance contrast and is therefore indicative of a relatively hard bed (encompassing materials from stiff sediment to bedrock). This occurs 700 ± 40 m upstream from station 1300. This is consistent with inferences made from surface topography, where the point of flotation is expected to be a short distance upstream of the topographic minimum (560 m upstream from station 1300, at station 1314), but is ~300 m upstream of the BedMachine picked grounding line. We image the seabed along two portions of the profile: from 0 to 300 m, and from 600 m to the grounding zone. Interference between the ice–water multiple and the seabed reflection results in ambiguity between these events at $x \simeq 200$ m; however, the dip and normal polarity of the seabed reflection enables its identification (the ice–base multiple has a reversed polarity). Taking an average velocity in the firn and ice of 3610 ± 30 ms^{-1} from short refraction surveys (Hoffman *et al.*, 2025), the ice thickness is 280 ± 10 m at the downstream end of the array and 258 ± 10 m at the upstream end. The ice thins to 233 ± 10 m as it crosses the grounding line. Assuming a seawater velocity of 1500 ms^{-1}, the water column thickness is 140 m beneath station 1300.

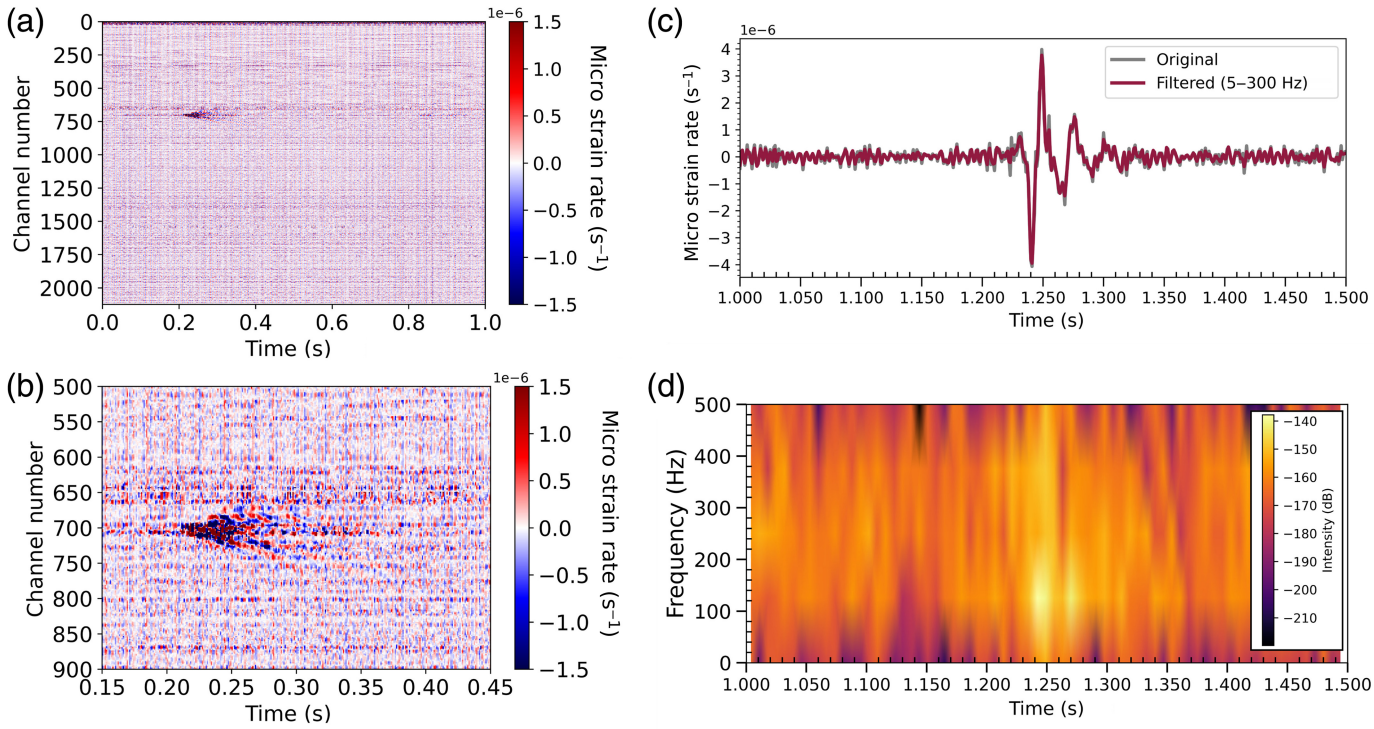

Figure 6. (a) One second of DAS strain-rate data recorded on 3.4 km of fiber-optic cable, showing one hammer strike. (b) Zoom of 0.3 s of the DAS data displayed in (a), from channels 500 to 900. Main cable layout is from channel 626. (c) Example trace from channel 719 (9.5 m source–receiver offset), displayed raw (gray line) and with a 5–300 Hz band-pass filter (red line). Sampling rate is 1 kHz. (d) Spectrogram for 0.5 s strain-rate data for channel 719. Displayed data are from the file EWG_ACTIVE_2024-02-06_23-53-07_UTC. The color version of this figure is available only in the electronic edition.

Where we do not image the seabed, there is a seabed elevation change of 80 m over a horizontal distance of 270 m, implying a steep dip of roughly 17°.

Analysis of active source data from the 3D acquisition (A2) will provide insights into the 3D structure and deformation of the grounding zone, including crystal orientation fabric, azimuthal anisotropy, and 3D bed topography. Tides at this site are small in the context of the Antarctic continent (~1.4 m); this fact combined with the steep bed topography leads us to expect little grounding line migration. This data set may therefore provide a useful control to study glaciological processes where the grounding zone geometry may be relatively static, and provide context for further studies in areas such as the Weddell Sea where grounding lines migrate large distances (e.g., Freer *et al.*, 2023).

Ambient noise analysis

Ambient noise techniques reconstruct virtual active sources at each station location by cross-correlating continuous seismic noise records between every pair of stations. Ambient noise processing followed Pearce *et al.* (2024). Optimization for ambient noise data acquisition ensured varying interstation distances to record waves of different frequencies that sample a wide range of depths. Over 54,000 Green's functions were extracted from nine days of recordings for interstation cross correlations, with interstation distances ranging from ~40 to 1200 m. We used continuous data from all 330 stations for nine days of recording between 13 and 21 January 2023. Data preprocessing involved down-sampling to 100 Hz and high-pass filtering at 0.04 Hz. Subsequently, the data were segmented into 15 min intervals. For each segment, processing was conducted to remove any impulsive events unrelated to the ambient noise field (e.g., volcanic or icequake signals).

Cross-correlation functions were computed in the frequency domain between all station pairs using the processed 15 min segments, following the approach of Bensen *et al.* (2007). Correlation functions from all segments in a day were averaged to obtain a single daily correlation function for each station pair. Nine intercomponent correlation functions corresponding to the elastic Green's tensor were computed. The Green's correlation tensor was rotated along the interstation azimuth to provide correlation functions between the radial (R), transverse (T), and vertical (Z) components (Fig. 8).

The observed arrivals primarily consist of dispersive surface waves traveling between station pairs; this is clear from the frequency dependence of the reconstructed wave velocity. Rayleigh waves are observed on the RR, ZZ, RZ, and ZR components, whereas Love waves are apparent on the TT correlation term.

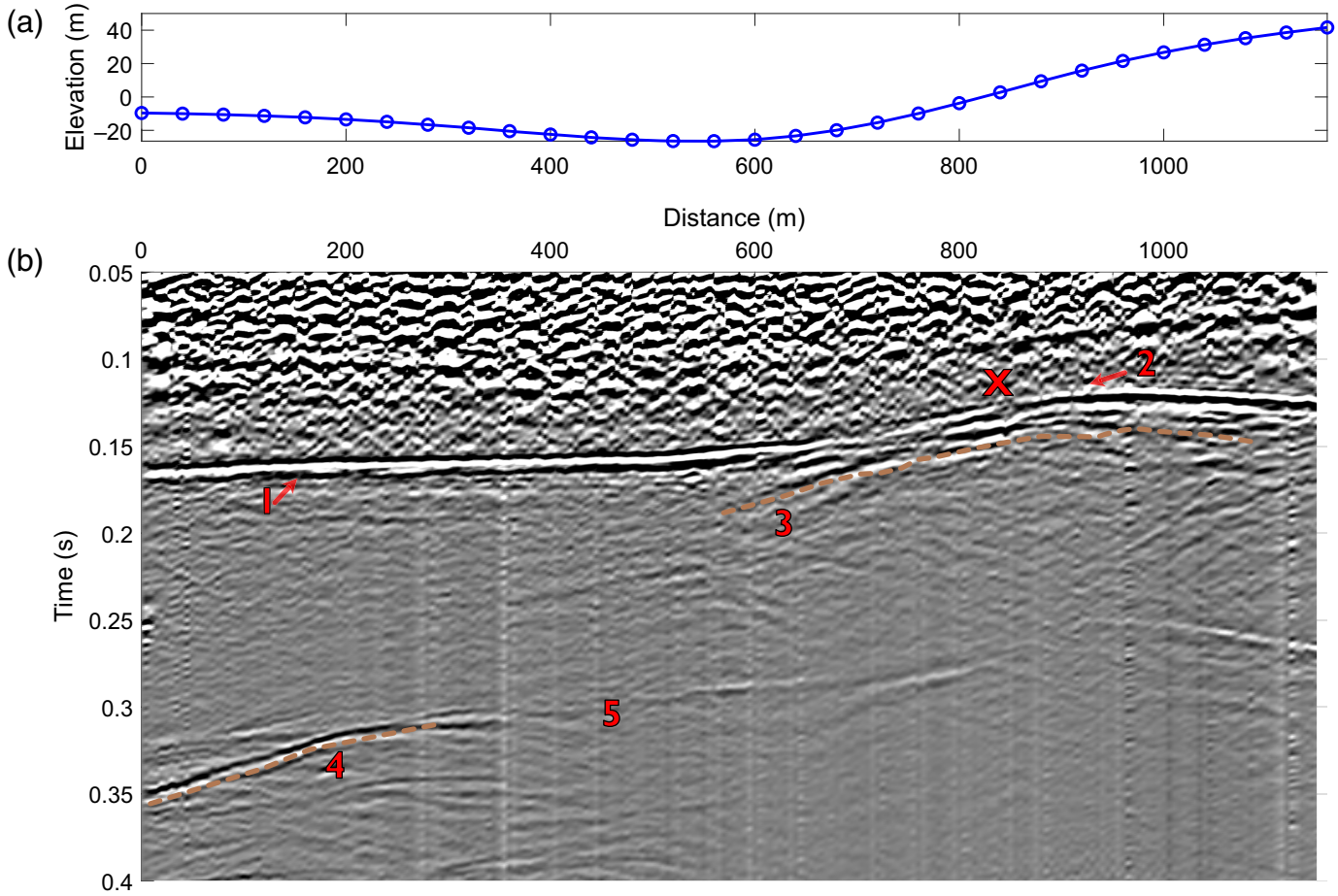

Figure 7. (a) Surface elevation over grounding zone from real-time kinematic (RTK) Global Positioning System (GPS) surveying. The circles indicate node locations. (b) Unmigrated time section of seismic data over the grounding zone. Time axis is two-way travel time. Features indicated are (1) ice–water interface, (2) ice–bedrock interface, (3) seabed close to grounding zone, (4) seabed beneath the ice shelf, and (5) ice–water multiple. "X" marks the location of the grounding line at time of survey. Interpreted seabed is marked with the overlaid line, with the central section hypothesized steeply dipping and not imaged. Apparent features arriving before the ice–base reflection consist of residual groundroll and *f-k* artefacts. Flow is right to left. The color version of this figure is available only in the electronic edition.

Icequake detection and location

Icequakes are seismic events generated from fracturing in the ice column or stick slip at the ice–bed interface. As shown in Figure 4, there were a variety of events detected by the EG array. We show here a more detailed example of one such event detected using QuakeMigrate (Winder *et al.*, 2022), using a 19-station subset of the array. QuakeMigrate calculates probable source locations by moving through the travel-time curves for both *P* and *S* waves. These locations and times are mapped into a common coordinate system to form a coalescence function—the maximum of the normalized coalescence represents the most likely event location. Figure 9 shows the output of QuakeMigrate for a single event detected at the EG array. Figure 9a shows the coalescence value in latitude/longitude, latitude/depth, and longitude/depth axes, locating the event to ∼100 m southeast of the array, at ∼50 m depth (i.e., in the ice column). Figure 9b shows waveforms for all three components, along with modeled compressional- and shear-wave arrival times. Figure 9c shows the maximum coalescence over time for this event pick.

We detect and locate events for a 24 hr period on 24 January 2023, on the 19-station subset of our array. We detect events between 5 and 120 Hz for *P*-wave arrivals and 5–50 Hz for *S*-wave arrivals. During this 24 hr period, ∼26,000 events were detected. Note that this catalog has not been robustly validated, so this is likely an overestimate. We cluster these events into bins of size 100 × 150 m. Figure 10 shows the event density (events per bin) for the period. The event density is high within the array (∼200 events per bin per day), but the highest density of events (>400 events per bin per day) coincides with the shear margin to the southeast of the array. This suggests that the data set contains abundant surface and crevassing events. Although we do not locate any volcanic events associated with the position of Mt Erebus, we expect this is due to the parameterization of QuakeMigrate, which was tuned for the detection of icequakes, which are of higher frequency than typical volcanic signals. Further analysis of

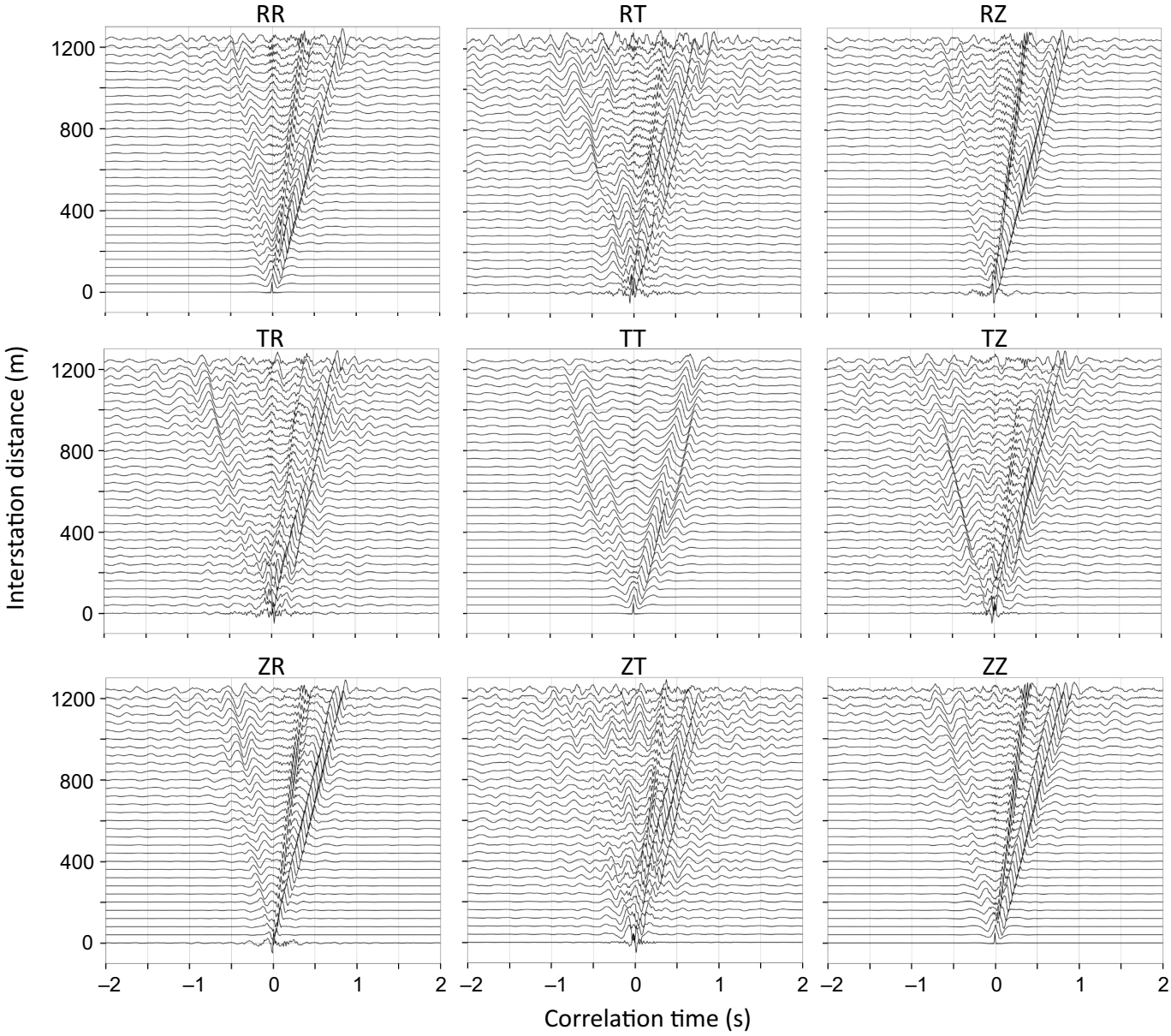

Figure 8. Correlograms obtained from the 54,000 interstation Green's functions, stacked based on interstation distance.

icequakes will allow the identification of basal events and may provide more information about the extent and character of tidal grounding line migration.

Summary

We have described data sets that comprise active and passive seismic surveys undertaken with a dense array of 330 seismic nodes in 2022/2023 and DAS in 2023/2024. This data set represents a comprehensive survey of the structure and seismic activity of a grounding zone over a tidal cycle. We have imaged the seabed downstream of the grounding zone and located the point of flotation using hammer-and-plate active seismics. The data set contains events from a variety of sources, including hammer shots, icequakes, and skidoos. Preliminary analysis of icequakes detected suggests a high proportion of surface events. Further analyses of these data sets will provide fundamental insights into grounding zone processes and the grounding zone's 3D structure, informing studies of grounding zone dynamics around the Antarctic continent.

Data and Resources

Node data have been archived at the Incorporated Research Institutions for Seismology (IRIS) Data Management Center (DMC) with the network code XS (Young *et al.*, 2023). Metadata are available at https://ds.iris.edu/mda/XS/?timewindow=2023-2023 (last accessed July 2025). Note stations 1334, 1335, and 1336 are timer nodes. 1335 and 1336 did not record all shots. The supplemental material includes one pdf file showing unprocessed receiver gathers and two csv files containing approximate shot times for the 2D and 3D active source surveys (acquisitions A1 and A2). Distributed acoustic sensing data are archived with the United Kingdom Natural Environment

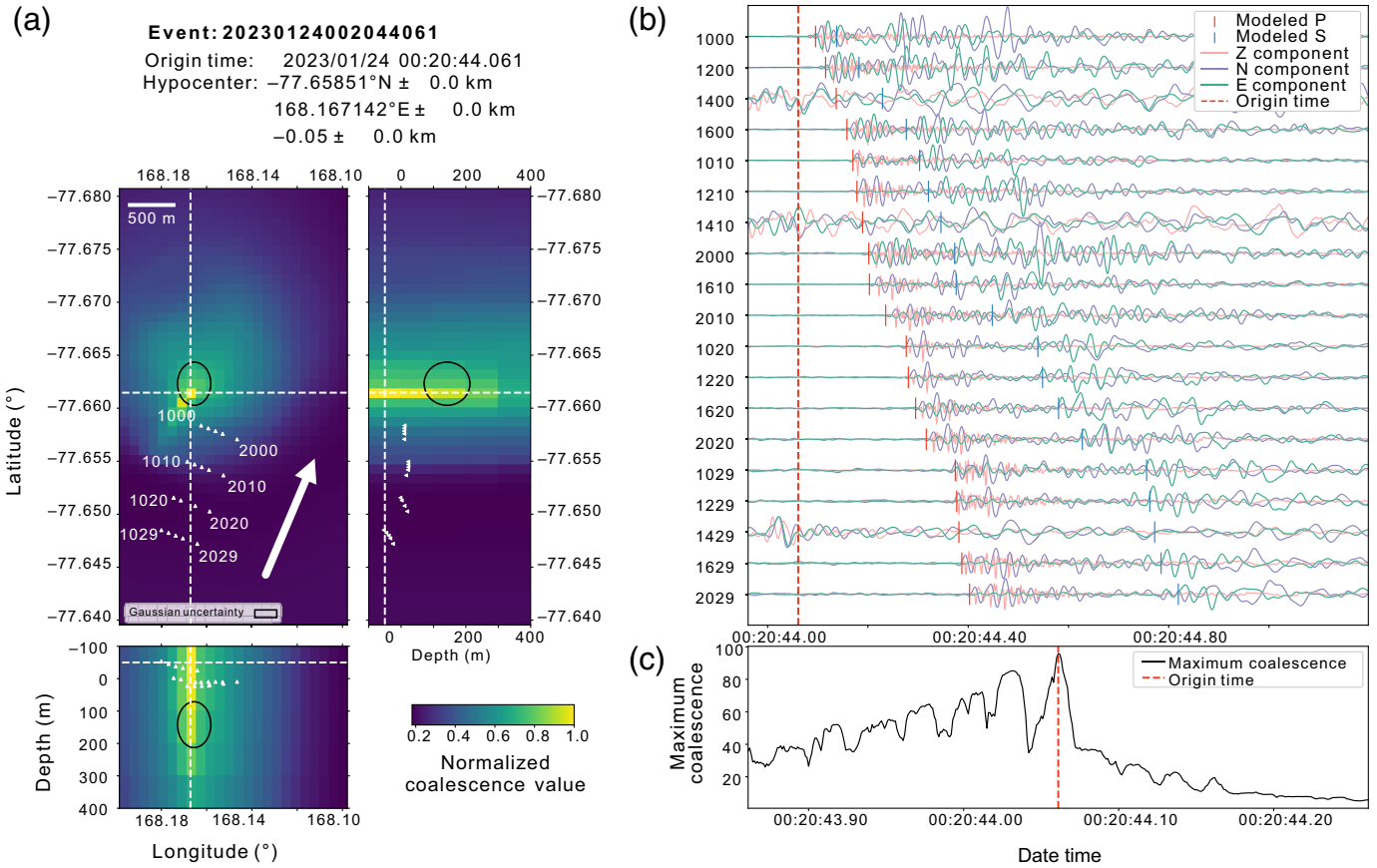

Figure 9. Output of Quakemigrate event detection and location for a single surface event. (a) An energy distribution map showing coalescence of a single event on all receivers. High normalized coalescence indicates the most likely source location and depth for the picked event. Ice flow direction is indicated by the arrow. (b) The modeled compressional (*P*)- and shear (*S*)-wave arrival time for the picked event used for the event location, shown alongside detected waveforms. (c) Maximum coalescence over time. The red dashed line shows the estimated origin time of the event. The color version of this figure is available only in the electronic edition.

Research Council (NERC) Polar Data Centre, doi: 10.5285/23dbd529-3a57-4933-bb9d-16ee1c85fda0.

Declaration of Competing Interests

The authors acknowledge that there are no conflicts of interest recorded.

Acknowledgments

Eastwind Glacier Geophysical Surveys on Top of an Antarctic Ice Shelf Transition (EGGS on TOAST) was supported through a National Science Foundation (NSF) Emerging Tasking Identification and is part of the Thwaites Interdisciplinary Margin Evolution (TIME) project, a component of the International Thwaites Glacier Collaboration (ITGC). Support from NSF (Grant 1739027) and Natural Environment Research Council (NERC: Grants NE/S006788/1 and NE/S00677X/1). Logistics were provided by NSF-U.S. Antarctic Program and NERC-British Antarctic Survey. ITGC Contribution Number ITGC-141. Preparatory surveys of Eastwind Glacier were conducted through the EAGER project (Project number NSF 2027579). Seismic instruments were provided by EarthScope Consortium through PASSCAL Polar Support Services, by the University of Texas at El Paso, and by the University of Oklahoma. The facilities of EarthScope Consortium are supported by NSF's Seismological Facility for the Advancement of Geoscience (SAGE) Award (Cooperative Support Agreement OPP-1851037). Geodetic instruments were provided by the GAGE Facility, operated by EarthScope Consortium, with support from NSF, National Aeronautics and Space Administration (NASA), and the U.S. Geological Survey (NSF Cooperative Agreement EAR-1724794). Febus Optics A1-R Distributed acoustic sensing interrogator was loaned from the University of Leeds Fibre Optic Facility, under loan Agreement UOL-FOF-0004. The authors acknowledge the support of the University of Wisconsin–Madison Automatic Weather Station Program for the AWS data (NSF Grant 2301362) and the Polar Geospatial Center for mapping support. S. E. S. performed initial processing of seismic reflection data as part of the MSc Exploration Geophysics at the University of Leeds. Seismic data were processed with Halliburton–Landmark ProMAX software under academic license to British Antarctic Survey. The authors thank Jenny Cunningham for logistical support and Kelly M. Brunt for facilitating implementation of the Emerging Tasking Identification; Greg Runyan, Ema Mayo, and Hannah Miner for assistance in the field; Knut Christianson, Andy Smith, and Galen Kaip for advising on data acquisition; Ash Goverman for advising

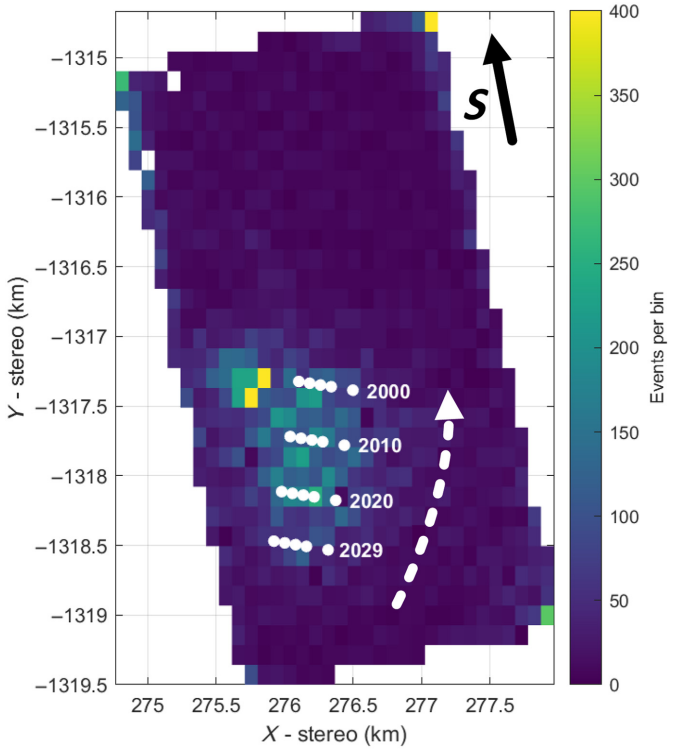

Figure 10. Event density for 1 day of data, 24 January 2023, clustered into 100 × 150 m bins. Approximately 26,000 seismic events were detected for the 24 hr period. The dashed arrow indicates ice flow direction. There is a high density of events in the shear margin southeast of the array. The color version of this figure is available only in the electronic edition.

on field planning. The authors are grateful to Florent Gimbert, Nicolas Paris, one anonymous reviewer, and the editor, whose feedback improved the article.

References

Anandakrishnan, S., and R. B. Alley (1997). Tidal forcing of basal seismicity of Ice Stream C, West Antarctica, observed far inland, *J. Geophys. Res.* **102,** no. B7, 15,183–15,196.

Anandakrishnan, S., D. Voigt, R. Alley, and M. King (2003). Ice stream D flow speed is strongly modulated by the tide beneath the Ross Ice Shelf, *Geophys. Res. Lett.* **30,** 1361.

Aster, R., S. Mah, P. Kyle, W. McIntosh, N. Dunbar, J. Johnson, M. Ruiz, and S. McNamara (2003). Very long period oscillations of Mount Erebus Volcano, *J. Geophys. Res.* **108,** 2522.

Begeman, C., S. Tulaczyk, L. Padman, M. King, M. Siegfried, T. Hodson, and H. Fricker (2020). Tidal pressurization of the ocean cavity near an Antarctic ice shelf grounding line, *J. Geophys. Res.* **125,** no. 4, doi: 10.1029/2019JC015562.

Behrendt, J. (1999). Crustal and lithospheric structure of the West Antarctic rift system from geophysical investigations—A review, *Global Planet. Change* **23,** nos. 1/4, 25–44.

Bensen, G., M. Ritzwoller, M. Barmin, A. L. Levshin, F. Lin, M. Moschetti, N. Shapiro, and Y. Yang (2007). Processing seismic ambient noise data to obtain reliable broad-band surface wave dispersion measurements, *Geophys. J. Int.* **169,** no. 3, 1239–1260.

Booth, A. D., P. Christoffersen, C. Schoonman, A. Clarke, B. Hubbard, R. Law, S. H. Doyle, T. R. Chudley, and A. Chalari (2020). Distributed acoustic sensing of seismic properties in a borehole drilled on a fast-flowing greenlandic outlet glacier. *Geophys. Res. Lett.* **47,** no. 13, e2020GL088148, doi: 10.1029/2020GL088148.

Brisbourne, A. M., T. S. Hudson, and J. M. Kendall (2024). *Borehole and Surface Applications of Distributed Acoustic Sensing for Characterization of the Cryosphere and Glacial Environments*, American Geophysical Union (AGU), Washington, D.C., 225–237.

Brisbourne, A. M., M. Kendall, S.-K. Kufner, T. S. Hudson, and A. M. Smith (2021). Downhole distributed acoustic seismic profiling at Skytrain Ice Rise, West Antarctica, *Cryosphere* **15,** no. 7, 3443–3458.

Brunt, K., H. Fricker, L. Padman, T. Scambos, and S. O'Neel (2010). Mapping the grounding zone of the Ross Ice Shelf, Antarctica, using ICESat laser altimetry, *Ann. Glaciol.* **51,** no. 55, 71–79.

Casey, R., M. E. Templeton, G. Sharer, L. Keyson, B. R. Weertman, and T. Ahern (2018). Assuring the quality of IRIS data with MUSTANG, *Seismol. Res. Lett.* **89,** no. 2A, 630–639.

Chaput, J., R. Aster, M. Karplus, N. Nakata, P. Gerstoft, P. Bromirski, A. Nyblade, R. Stephen, and D. Wiens (2023). Near-surface seismic anisotropy in Antarctic glacial snow and ice revealed by high-frequency ambient noise, *J. Glaciol.* **69,** no. 276, 773–789.

Christianson, K., B. Parizek, R. Alley, H. Horgan, R. Jacobel, S. Anandakrishnan, B. Keisling, B. Craig, and A. Muto (2013). Ice sheet grounding zone stabilization due to till compaction, *Geophys. Res. Lett.* **40,** 5406–5411.

Conway, H., B. Ball, G. H. Denton, A. Gades, and E. Waddington (1999). Past and future grounding-line retreat of the West Antarctic ice sheet, *Science* **286,** 280–283.

Davis, P., K. Nicholls, D. M. Holland, B. E. Schmidt, P. Washam, K. L. Riverman, R. J. Arthern, I. Vaňková, C. Eayrs, J. A. Smith, *et al.* (2023). Suppressed basal melting in the eastern Thwaites Glacier grounding zone, *Nature* **614,** 479–485.

Dibble, R., P. Kyle, and C. Rowe (2008). Video and seismic observations of Strombolian eruptions at Erebus volcano, Antarctica, *J. Volcanol. Geotherm. Res.* **177,** 619–634.

Drews, R., C. Wild, O. Marsh, W. Rack, T. Ehlers, N. Neckel, and V. Helm (2021). Grounding-zone flow variability of Priestley Glacier, Antarctica, in a diurnal tidal regime, *Geophys. Res. Lett.* **48,** e2021GL093853, doi: 10.1029/2021GL093853.

Fichtner, A., C. Hofstede, L. Gebraad, A. Zunino, D. Zigone, and O. Eisen (2023). Borehole fibre-optic seismology inside the Northeast Greenland Ice Stream, *Geophys. J. Int.* **235,** no. 3, 2430–2441.

Fichtner, A., C. Hofstede, B. L. N. Kennett, N. F. Nymand, M. L. Lauritzen, D. Zigone, and O. Eisen (2023). Fiber-optic airplane seismology on the northeast Greenland Ice Stream, *Seism. Rec.* **3,** no. 2, 125–133.

Fichtner, A., C. Hofstede, B. L. N. Kennett, A. Svensson, J. Westhoff, F. Walter, J.-P. Ampuero, E. Cook, D. Zigone, D. Jansen, *et al.* (2025). Hidden cascades of seismic ice stream deformation, *Science* **387,** no. 6736, 858–864.

Freer, B. I. D., O. J. Marsh, A. E. Hogg, H. A. Fricker, and L. Padman (2023). Modes of Antarctic tidal grounding line migration revealed by Ice, Cloud, and land elevation satellite-2 (ICESat-2) laser altimetry, *Cryosphere* **17,** no. 9, 4079–4101.

Fricker, H., R. Coleman, L. Padman, T. Scambos, J. Bohlander, and K. Brunt (2009). Mapping the grounding zone of the Amery Ice Shelf, east Antarctica using InSAR, MODIS and ICESat, *Antarct. Sci.* **21,** 515–532.

Gimbert, F., U. Nanni, P. Roux, A. Helmstetter, S. Garambois, A. Lecointre, A. Walpersdorf, B. Jourdain, M. Langlais, O. Laarman, *et al.* (2021). A multi-physics experiment with a temporary dense seismic array on the Argentière Glacier, French Alps: The RESOLVE project, *Seismol. Res. Lett.* **92,** no. 2A, 1185–1201.

Graham, A., A. Wahlin, K. A. Hogan, F. O. Nitsche, K. J. Heywood, R. L. Totten, J. A. Smith, C. D. Hillenbrand, L. M. Simkins, J. B. Anderson, *et al.* (2022). Rapid retreat of Thwaites Glacier in the pre-satellite era, *Nature Geosci.* **15,** 706–713.

Gudmundsson, G., J. Krug, G. Durand, L. Favier, and O. Gagliardini (2012). The stability of grounding lines on retrograde slopes, *Cryosphere* **6,** 1497–1505.

Haseloff, M., and O. Sergienko (2022). Effects of calving and submarine melting on steady states and stability of buttressed marine ice sheets, *J. Glaciol.* 1–18.

Hoffman, A. O., K. Christianson, M. S. Karplus, R. S. Agnew, E. Pearce, M. Ranganathan, S. Anandakrishnan, S. A. Cortez, M. Beres, R. Bingham, *et al.* (2025). Geophysical surveys and instrument incubation program across a glacier grounding zone: Eastwind Glacier's contribution to McMurdo ice shelf mass balance, ESS Open Archive, doi: 10.22541/essoar.173687398.85162904/v1.

Horgan, H., L. van Gaastrecht, R. Alley, S. Anandakrishnan, L. Beem, K. Christianson, A. Muto, and M. Siegfried (2021). Grounding zone subglacial properties from calibrated active-source seismic methods, *Cryosphere* **15,** 1863–1880.

Howat, I. M., C. Porter, B. E. Smith, M.-J. Noh, and P. Morin (2019). The reference elevation model of Antarctica, *Cryosphere* **13,** no. 2, 665–674.

Hudson, T. S., A. F. Baird, J. M. Kendall, S. K. Kufner, A. M. Brisbourne, A. M. Smith, A. Butcher, A. Chalari, and A. Clarke (2021). Distributed acoustic sensing (DAS) for natural microseismicity studies: A case study from Antarctica, *J. Geophys. Res.* **126,** no. 7, e2020JB021493, doi: 10.1029/2020JB021493.

Hughes, T. (1975). The West Antarctic Ice Sheet: Instability, disintegration, and initiation of ice ages, *Rev. Geophys.* **13,** 502–526.

Hulbe, C. L., M. Klinger, M. Masterson, G. Catania, K. Cruikshank, and A. Bugni (2016). Tidal bending and strand cracks at the kamb ice stream grounding line, West Antarctica, *J. Glaciol.* **62,** no. 235, 816–824.

Jenkins, A., D. Shoosmith, P. Dutrieux, S. Jacobs, T. Kim, S. Lee, H. Ga, and S. Stammerjohn (2018). West Antarctic Ice Sheet retreat in the Amundsen Sea driven by decadal oceanic variability, *Nature Geosci.* **11,** 733–738.

Joughin, I., B. Smith, and B. Medley (2014). Marine ice sheet collapse potentially under way for the Thwaites Glacier basin, *West Antarctica Sci.* **344,** 735–738.

Karplus, M., and B. Schmandt (2018). Preface to the focus section on geophone array seismology, *Seismol. Res. Lett.* **89,** no. 5, 1597–1600.

Karplus, M. S., N. Nakata, G. M. Kaip, S. H. Harder, L. F. Gonzalez, A. D. Booth, E. C. Smith, S. A. Veitch, J. I. Walter, and P. Christoffersen (2024). Signal characteristics of surface seismic explosive sources near the West Antarctic Ice Sheet divide, *J. Glaciol.* **70,** e16.

Lazzara, M. A., G. A. Weidner, L. M. Keller, J. E. Thom, and J. J. Cassano (2012). Antarctic automatic weather station program: 30 years of polar observation, *Bull. Am. Meteorol. Soc.* **93,** no. 10, 1519–1537.

Le Bris, T., G. Barruol, F. Gimbert, E. Le Meur, D. Zigone, A. Togaibekov, and D. Lombardi (2024). Spatial and temporal variability in tide-induced icequake activity at the Astrolabe Glacier, East Antarctica, ESS Open Archive, doi: 10.22541/essoar.173324864.46462523/v1.

Longuet-Higgins, M. (1950). A theory of the origin of microseisms, *Phil. Trans. Roy. Soc. Lond. A* **243,** no. 857, 1–35.

Lucas, E. M., A. A. Nyblade, R. C. Aster, D. A. Wiens, T. J. Wilson, J. P. Winberry, and A. D. Huerta (2023). Tidally modulated glacial seismicity at the Foundation Ice Stream, West Antarctica, *J. Geophys. Res.* **128,** no. 7, e2023JF007172, doi: 10.1029/2023JF007172.

McNamara, D., and R. Buland (2004). Ambient noise levels in the continental united states, *Bull. Seismol. Soc. Am.* **94,** no. 4, 1517–1527.

Minowa, M., E. A. Podolskiy, and S. Sugiyama (2019). Tide-modulated ice motion and seismicity of a floating glacier tongue in East Antarctica, *Ann. Glaciol.* **60,** no. 79, 57–67.

Morlighem, M., E. Rignot, T. Binder, D. Blankenship, R. Drews, G. Eagles, O. Eisen, F. Ferraccioli, R. Forsberg, and P. Fretwell, *et al.* (2020). Deep glacial troughs and stabilizing ridges unveiled beneath the margins of the Antarctic ice sheet, *Nature Sci.* 13**,** 132–137, doi: 10.1038/s41561-019-0510-8.

Morlighem, M., E. Rignot, T. Binder, D. Blankenship, R. Drews, G. Eagles, O. Eisen, F. Ferraccioli, R. Forsberg, P. Fretwell, *et al.* (2020). Deep glacial troughs and stabilizing ridges unveiled beneath the margins of the Antarctic ice sheet, *Nature Geosci.* **13,** no. 2, 132–137.

Nanni, U., F. Gimbert, P. Roux, and A. Lecointre (2021). Observing the subglacial hydrology network and its dynamics with a dense seismic array, *Proc. Natl. Acad. Sci. Unit. States Am.* **118,** no. 28, e2023757118, doi: 10.1073/pnas.2023757118.

Nanni, U., P. Roux, F. Gimbert, and A. Lecointre (2022). Dynamic imaging of glacier structures at high-resolution using source localization with a dense seismic array, *Geophys. Res. Lett.* **49,** no. 6, e2021GL095996, doi: 10.1029/2021GL095996.

Neuhaus, S. U., S. M. Tulaczyk, N. D. Stansell, J. J. Coenen, R. P. Scherer, J. A. Mikucki, and R. D. Powell (2021). Did holocene climate changes drive West Antarctic grounding line retreat and readvance? *Cryosphere* **15,** no. 10, 4655–4673.

Padman, L., H. A. Fricker, R. Coleman, S. Howard, and L. Erofeeva (2002). A new tide model for the Antarctic ice shelves and seas, *Ann. Glaciol.* **34,** 247–254.

Pearce, E., D. Zigone, C. Hofstede, A. Fichtner, J. Rimpot, S. O. Rasmussen, J. Freitag, and O. Eisen (2024). Firn seismic anisotropy in the northeast Greenland Ice Stream from ambient-noise surface waves, *Cryosphere* **18,** no. 10, 4917–4932.

Peterson, J. (1993). Observations and modeling of seismic background noise, *U.S. Geol. Surv. Open-File Rept. 93-322*, 94 pp.

Podolskiy, E. A., S. Sugiyama, M. Funk, F. Walter, R. Genco, S. Tsutaki, M. Minowa, and M. Ripepe (2016). Tide-modulated ice flow variations drive seismicity near the calving front of Bowdoin Glacier, Greenland, *Geophys. Res. Lett.* **43,** no. 5, 2036–2044.

Reese, R., J. Garbe, E. Hill, B. Urruty, K. Naughten, O. Gagliardini, G. Durand, F. Gillet-Chaulet, G. Gudmundsson, D. Chandler, *et al.* (2023). The stability of present-day Antarctic grounding lines - Part 2: Onset of irreversible retreat of Amundsen Sea glaciers under current climate on centennial timescales cannot be excluded, *Cryosphere* **17,** 3761–3783.

Rignot, E., M. Mouginot, M. Morlighem, H. Seroussi, and B. Scheuchl (2014). Widespread, rapid grounding line retreat of Pine Island, Thwaites, Smith, and Kohler glaciers, West Antarctica, from 1992 to 2011, *Geophys. Res. Lett.* **41,** 3502–3509.

Robel, A., C. Schoof, and E. Tziperman (2014). Rapid grounding line migration induced by internal ice stream variability, *J. Geophys. Res.* **119,** 2430–2447.

Rowe, C., R. Aster, P. Kyle, R. Dibble, and J. Schlue (2000). Seismic and acoustic observations at Mount Erebus Volcano, Ross Island, Antarctica, *J. Volcanol. Geotherm. Res.* **101,** 105–128.

Schoof, C. (2007). Ice sheet grounding line dynamics: Steady states, stability, and hysteresis, *J. Geophys. Res.* **112,** F03S28, doi: 10.1029/2006JF000664.

Stern, T., F. Davey, and G. Delisle (1991). Lithospheric flexure induced by the load of the Ross archipelago, southern Victoria Land, Antarctica, *Proceedings of the Fifth International Symposium on Antarctic Earth Sciences*, Cambridge, August 1987, 323–328.

van Ginkel, J., F. Walter, F. Lindner, M. Hallo, M. Huss, and D. Fäh (2025). Spectral characteristics of seismic ambient vibrations reveal changes in the subglacial environment of glacier de la plaine morte, switzerland, *Cryosphere* **19,** no. 3, 1469–1490.

Veitch, S. A., M. Karplus, G. Kaip, L. F. Gonzalez, J. M. Amundson, and T. C. Bartholomaus (2021). Ice thickness estimates of Lemon Creek Glacier, Alaska, from active-source seismic imaging, *J. Glaciol.* **67,** no. 265, 824–832.

Weertman, J. (1974). Stability of the junction of an ice sheet and an ice shelf, *J. Glaciol.* **13,** 3–13.

Winder, T., C. Bacon, J. Smith, T. Hudson, T. Greenfield, and R. White (2022). QuakeMigrate: A modular, open-source python package for automatic earthquake detection and location, Authorea, doi: 10.1002/essoar.10505850.1.

Young, T. J., R. Agnew, M. Hunt, E. Pearce, and M. Karplus (2023). *Eastwind Glacier Geophysical Surveys on Top Of Antarctic iceShelf Transition* [Data Set], International Federation of Digital Seismograph Networks, doi: 10.7914/jah0-9856.

Zoet, L. K., S. Anandakrishnan, R. B. Alley, A. A. Nyblade, and D. A. Wiens (2012). Motion of an Antarctic glacier by repeated tidally modulated earthquakes, *Nature Geosci.* **5,** no. 9, 623–626.

Manuscript received 17 January 2025
Published online 22 August 2025